Significant performance improvement in terms of reduced cathode flooding in polymer electrolyte fuel cell using a stainless-steel microcoil gas flow field

Shiro Tanaka [a,b,*], Toshio Shudo [a]

[a] Department of Mechanical Engineering, Tokyo Metropolitan University, 1 Minamiosawa, Hachioji, Tokyo 192-0397, Japan
[b] HySA/Catalysis, Department of Chemical Engineering, University of Cape Town, Private Bag X3, Rondebosch, Cape Town 7701, South Africa

HIGHLIGHTS

- We achieve flood-free performance using aligned microcoils as a flow field.
- The GDL has no observable effect on flooding if air is uniformly distributed.
- The HFR is high in GDL-less design with less contact point of the microcoils.
- The membrane is dehydrated in high current density with big temperature raise.

ARTICLE INFO

ABSTRACT

Flooding at the cathode is the greatest barrier to increasing the power density of polymer electrolyte fuel cells (PEFCs) and using them at high current densities. Previous studies have shown that flooding is caused by water accumulation in the gas diffusion layer, but only a few researchers have succeeded in overcoming this issue. In the present study, microcoils are used as the gas flow channel as well as the gas diffuser directly on the microporous layer (MPL), without using a conventional carbon-fiber gas diffusion layer (GDL), to enable flood-free performance. The current–voltage curves show flooding-free performance even under low air stoichiometry. However, the high-frequency resistance (HFR) in this case is slightly higher than that in grooved flow channels and GDLs. This is due to the differences in the electron conduction path, and the in-plane electron conductivity in the MPL is the key to enhancing the microcoil fuel cell performance.

© 2013 Elsevier B.V. All rights reserved.

1. Introduction

Polymer electrolyte fuel cells (PEFCs), which convert the chemical energy of hydrogen directly into electrical energy, are regarded as a promising alternative clean power source for automotive, stationary, and portable applications [1–5]. The acceptance of fuel cells for automotive use requires reduction in their cost and size, as current automotive fuel cells are not yet profitable and are still too large, putting limitations on the layout of the fuel cell system [6].

Currently, most automotive fuel cells are operated at a maximum current density of 1.0 A cm^{-2} [7–9]. This low current density requires a large active area in order to produce a vehicle power output of 70–120 kW, which necessarily increases the number of polymer electrolyte membranes (e.g., Nafion, Acipex, and Dow membrane), catalyst layers with precious metals, and gas diffusion layers (GDLs). The expense of these materials means that enlarging the active area significantly increases the cost of fuel cell stack. In addition, the thickness of the GDL at 90–200 μm for each electrode increases the length in the stacking direction, as the total volume of the GDL occupies about half of the fuel cell stack. These considerations create limitations for conventional fuel cell structures with regard to cost and size.

Solving these commercialization issues for automotive fuel cells requires a novel fuel cell structure that enables high current density

* Corresponding author. HySA/Catalysis, Department of Chemical Engineering, University of Cape Town, Private Bag X3, Rondebosch, Cape Town 7701, South Africa. Tel.: +27 21 650 3852; fax: +27 21 650 5509.
E-mail address: shiro.tanaka@uct.ac.za (S. Tanaka).

operation without a GDL. Increasing the current density of conventional fuel cells causes them to undergo a sudden decrease in performance, known as cathode flooding. When current density increases, more water is generated in the electrochemical reaction $(O_2 + 4H^+ + 4e^- \rightarrow 2H_2O)$ at the cathode, and more water is transported from the anode to the cathode through the membrane via electro-osmotic drag [10–12]. The water at the cathode condenses and accumulates, blocking oxygen diffusion and causing a sudden decrease in the cell voltage.

Simultaneously, increasing the current density causes the membrane to dry out at the anode. The membrane is dehydrated by electro-osmotic drag from the anode to the cathode, decreasing the water concentration [13]. The increased temperature arising from the electrochemical reaction and the ohmic heat also dehydrate the membrane. The proton conductivity of the membrane heavily depends on its water content, meaning that dehydration of the membrane decreases proton conductivity and thus cell performance.

There are a few reports on efforts to overcome membrane flooding/dry-out. Shudo et al. replaced the conventional land/channel flow field structure with a porous stainless steel in direct methanol fuel cell (DMFC) operations [14]. Using electrochemical impedance spectroscopy (EIS), they found that their fuel cell with a porous flow field allowed for uniform distribution of the reactant gas onto the catalyst layer, thus enabling higher performance than that of conventional cells even at a high current density of 0.5 A cm^{-2}. Strickland et al. developed a unique flow field with in-situ polymerized wicks coated onto the cathode channel in a hydrogen fuel cell [15]. The performance of their cell design was flood-free even at 1.5 A cm^{-2}. They concluded that the cathode channel wick provided a hydraulic pathway from the reaction sites to the outside of the fuel cell that removed the product water and diffused oxygen to the catalyst layers. Turhan et al. explored the effect of changing the width ratio of the land and channel (L/C) on water accumulation using an in-situ neutron imaging technique [16]. They concluded that liquid water tended to accumulate under the lands rather than under the channels, and that accumulation depended strongly on the flow-field geometry. As L/C decreased, less liquid water accumulated in the cell, permitting higher cell performance with less flooding.

While there are a few published studies on flow-field alterations for extending current densities, there is little in the literature suggesting novel structures or materials to overcome flooding and dry-out with smaller cells and lower pressure drop designs. In this report, we describe a unique fuel cell design that utilizes stainless steel microcoils to generate the flow field and gas diffusion layer. We compared the fuel cell performance of microcoils with and without a GDL and conventional flow fields with a GDL under various conditions, and discussed how the microcoils in the fuel cell reduced flooding and dry-out. In addition, these new structures and materials were expected to perform differently compared with conventional structures and materials, and so we subsequently characterized the electrical and thermal properties of several elements of the fuel cells.

2. Experimental

2.1. Fuel cell preparation

The bipolar plates for our fuel cell had 5 cm^2 active areas (1 cm × 5 cm) made of graphite (Mechanical Carbon Industry, Kanagawa, Japan). The end-plates for these bipolar plates were made with stainless steel, with eight holes for fastening the fuel cell with a compression pressure of 1 MPa. The end-plates had sheet heaters on the outside of both the anode and cathode to control the cell temperature. A stainless steel current-collector with 1-μm-thick gold-plate was inserted between the bipolar plate and the end-plate on both sides. 0.6 mm-thick Ethylene–propylene diene monomer rubber (EPDM) gaskets (NOK Corp, Tokyo, Japan) were used to surround the active area and seal the reactant gases. Bolt torques of 0.3 N m were used to achieve the compression pressure of 1.0 MPa for the fuel cell assembly.

25-μm-thick Nafion (NRE211, du Pont de Nemours, Delaware, USA) was chosen as a polymer electrolyte membrane, and carbon-supported platinum (Pt/C, 50 wt% Pt, TEC10E50E, Tanaka K.K., Tokyo, Japan) was selected as a catalyst. The catalyst-coated membrane (CCM) was prepared as follows: Pt/C powder was mixed with a Nafion dispersion (DE2020 du Pont de Nemours, Delaware, USA) using a zirconia bead mill for 8 h on a rotation table. The diameter of the beads was 1 mm, and the speed of rotation of the table was 400 rpm. The solid contents of the catalyst were prepared using a 1:1 mixture of carbon support:Nafion-ionomer. The catalyst was coated on both sides of the membrane with a spray coater (Mic Lab, Kanagawa, Japan) several times until the coating thickness was about 30 μm. The platinum loadings were 0.4 mg cm^{-2} for both the anode and the cathode. The coated membrane was dried at 80 °C for 60 min and annealed at 130 °C for 10 min to obtain the CCM.

Microporous layers (MPLs) were used in the anode and cathode catalyst layers to control the water management of the fuel cell [17]. MPLs were prepared as follows: powdered carbon black (CB; Denka Black, Denki Kagaku Kogyo K.K., Tokyo, Japan), polytetrafluoroethylene (PTFE) aqueous dispersions (D-1, Daikin Industries Ltd., Osaka, Japan), nonionic surfactant (Triton X-100, Sigma–Aldrich), and DI water were mixed with 1 mm zirconia beads in a bead mill for 3 h at 400 rpm using 5:1:20:20 CB:PTFE:surfactant:water. This coating was cast onto an expanded PTFE porous sheet (30 μm thick, Poreflon Membrane, Sumitomo Electric Industries Ltd., Osaka, Japan) and dried at 350 °C for 60 min to obtain MPLs 40 μm and 60 μm thick.

The CCM was hot-pressed with MPLs on both sides for the anode and cathode at 130 °C and 3 MPa g for 10 min, using 200 μm-thick Teflon backing sheets on both sides to avoid MPL attachment to the plates of the hand-press.

The cathode was chosen for these experiments because the cathode reaction has been found to be the limiting step in PEFCs, in contrast to the fast kinetics of the anode reaction as demonstrated by Springer et al. in their EIS study [18].

We evaluated four designs of cathode flow fields in this study. The first design was a conventional flow field, with a cathode land 50 mm long and 1 mm wide, and cathode channels 50 mm long, 1 mm wide, and 1 mm deep. The GDL was laid between the flow field and MPL at the cathode (Design 1; conventional flow field with GDL). The second design utilized a microcoil with a 0.6 mm outer diameter and a GDL (280 μm thick, 5 wt% PTFE, TGP-H-090, Toray, Tokyo, Japan) between the microcoil and the MPL on the cathode side (Design 2; 0.6 mm microcoil with GDL). The third and fourth designs both featured microcoil flow fields tightly arranged parallel to the cathode air flow on pool-shaped graphite bipolar plates. Both microcoils were purchased from Micro Spring K.K. (Nagano, Japan) and were made of 50-μm stainless steel fiber with 0.1-μm-thick gold plating. The pitch of the coil was 90 μm, and the width of the opening was 40 μm; this configuration prevented the fibers from getting entangled with one other and facilitated the tight arrangement of the microcoils. The outer diameter of the microcoil for the third design was 0.6 mm (Design 3; 0.6 mm microcoil), and that for the fourth design was 0.2 mm (Design 4; 0.2 mm microcoil). The microcoils for both designs were directly laid on the cathode MPLs without a GDL.
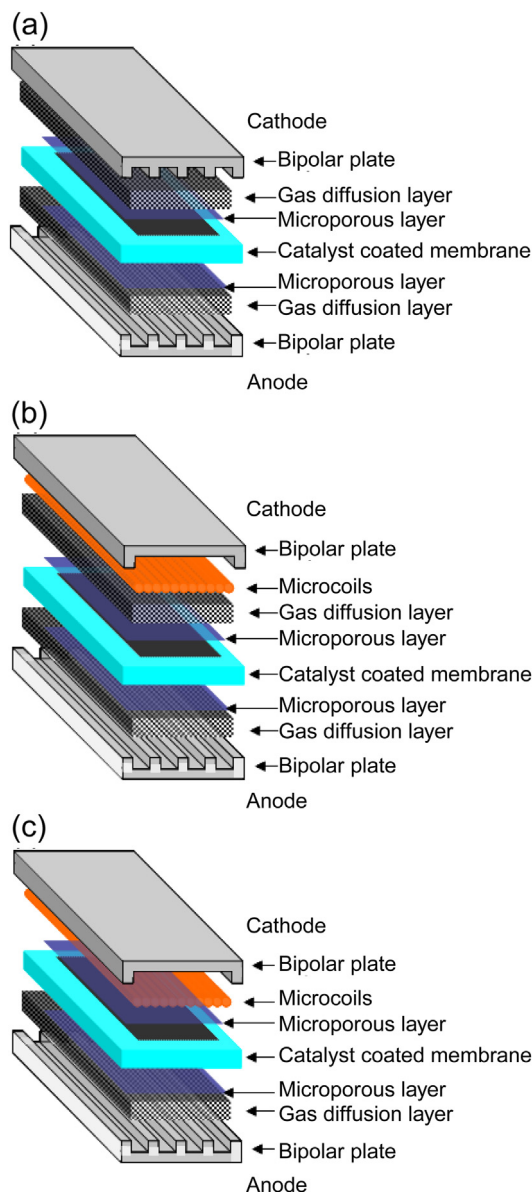
Fig. 1. Schematic image of (a) 0.2 mm or 0.6 mm microcoils without a GDL, (b) ø 0.6 mm microcoil with a GDL, and (c) conventional flow field with a GDL. In all the designs, the anode was a conventional flow field.

We used a conventional flow field for the anode in all the designs in order to focus on the effects on the cathode. The anode land was 50 mm long and 1 mm wide, and the anode channels were 50 mm long, 1 mm wide, and 1 mm deep. The GDL was laid

Table 1
MEA and flow field configuration of each design.

	Flow field		GDL		MPL	
	Anode	Cathode	Anode	Cathode	Anode	Cathode
Design 1	Conventional	Conventional	TGP-H-090	TGP-H-090	40 μm	40 μm
Design 2	Conventional	0.6 mm microcoil	TGP-H-090	TGP-H-090	40 μm	40 μm
Design 3	Conventional	0.6 mm microcoil	TGP-H-090	None	40 μm	40 μm
Design 4	Conventional	0.2 mm microcoil	TGP-H-090	None	40 μm	40 μm

between the anode bipolar plate and the MPL. Fig. 1 shows a schematic of the flow fields evaluated, and Table 1 shows the configuration of the corresponding fuel cells. Fig. 2 shows a schematic image of the microcoil and an actual picture of the microcoils and bipolar plate assembly.

2.2. Characterization of fuel cell performance

The single cells were mounted on a fuel cell test stand (Chino Corp., Tokyo, Japan) equipped with mass-flow controllers, an electronic loading device (Kikusui Electronics Corp., Yokohama, Japan) for controlling the electric current, an AC milliohm tester (Model 3566, Tsuruga Electric Corp., Osaka, Japan) with a constant high frequency resistance (HFR) of 1 kHz, and a computer for equipment monitoring and data collection. All the voltage, current, and resistance data were averaged from the logged data in 0.1 s for 10 min continual operation under each set of conditions.

To measure the polarization curves, gas flows for the anode and cathode were held constant; 0.42 L min^{-1} of pure hydrogen was supplied to the anode (stoichiometry: 9.0 at 1.5 A cm^{-2}), and 1.04 L min^{-1} of air was supplied to the cathode (stoichiometry: 9.0 at 1.5 A cm^{-2}). All reaction gases were humidified to 100% relative humidity (RH) with temperature-controlled water bubbling tanks. The fuel cell temperature was maintained at 70 °C with the heater and thermocouples inserted into the cathode bipolar plate.

For stoichiometry-dependent measurements, the gas flow to the anode was maintained at 0.21 L min^{-1} and the cathode gas stoichiometry was varied from 30.0 to 1.05 at 1.0 A cm^{-2} with 100% humidified air at 70 °C generated using the water bubbling tanks.

All power generation processes were conducted under atmospheric conditions. All fuel cell evaluations were conducted after 10 h of aging at a current density of 1.0 A cm^{-2}, a temperature of 70 °C, an anode feed gas flow of 0.5 L min^{-1} with 100% humidified hydrogen, and a cathode feed gas flow of 0.5 L min^{-1} with 100% humidified air.

2.3. In-plane and through-plane electronic resistivity

For our fuel cells, the electron-conducting pathway from the cathode catalyst to the bipolar plate was thought to be different
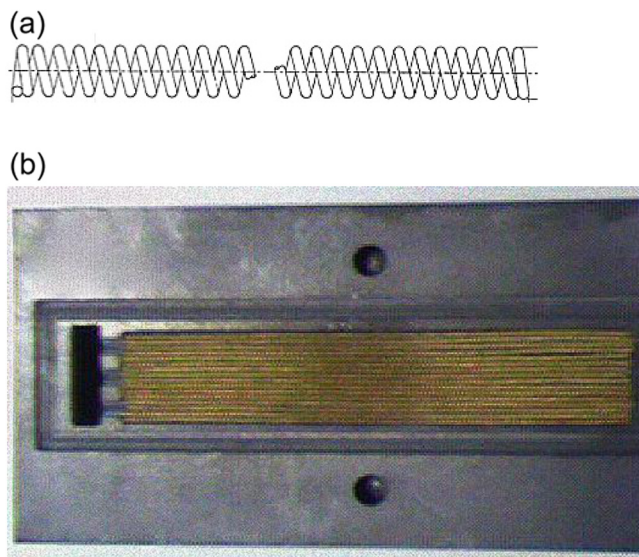

Fig. 2. Schematic image and actual picture of (a) microcoil and (b) microcoils and bipolar plate assembly.

from conventional fuel cells and thus was expected to lead to different HFRs. For example, electrons in Designs 1 and 2 were transferred from the catalyst layer through the MPL vertically to the GDL because the GDL covered the entire active area uniformly. In Designs 3 and 4, without a GDL, electrons in the catalyst layer first transferred vertically to the MPL and then moved horizontally within the MPL to the contact point of the microcoil. To characterize this, we measured the electronic resistivity of the GDL and MPL in the in-plane and through-plane directions.

The measurement of the in-plane resistivity was conducted at 25 °C following the standard ASTM C611 method, using four-point detectors in a direct current. 0.5 cm × 4.0 cm sample strips of the MPL and GDL were used. Resistances obtained with a resistance meter (1750 LCR Dig-Bridge with Kelvin clip leads, Quad Tech Inc., Maynard, USA) were converted to resistivity using the sample geometries.

The measurement of the through-plane resistivity was conducted at 25 °C in accordance with the method described in Ref. [19]. A 20 mm round sample was placed on a load cell (Electro-Puls™ E1000, Instron, Massachusetts, USA) between two gold-plated pedestals, and the sample was subjected to a compression pressure of 1 MPa. The same resistance meter as above was used to obtain the resistance of the sample. After the compression stress stabilized (30–60 min), the resistance was measured and converted to resistivity using the sample geometry.

2.4. Thermal resistance evaluation of GDL and microcoils

As with the electrical resistance, Designs 2–4 were thought to have thermal resistances different from those of conventional fuel cells, causing different degrees of temperature increases at a high current density, which could affect membrane dry-out. To characterize this, the thermal resistance and resistivity of the GDL and the microcoil were measured. Fig. 3 shows a schematic outlining the apparatus used for characterizing the thermal resistance of the GDL and microcoil. In this configuration, similar to that used by G. Karimi et al. [20] and Grant Unsworth [21], four
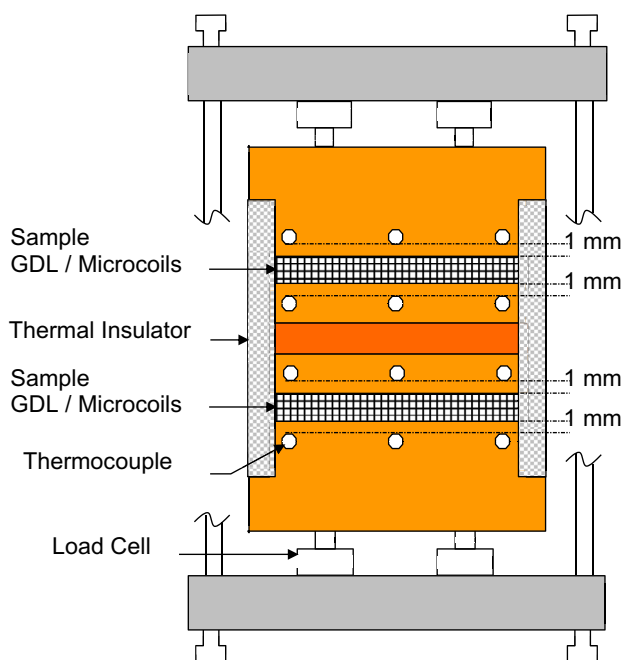

Fig. 3. Schematic image of depicting the test setup for the thermal conductivity measurements.
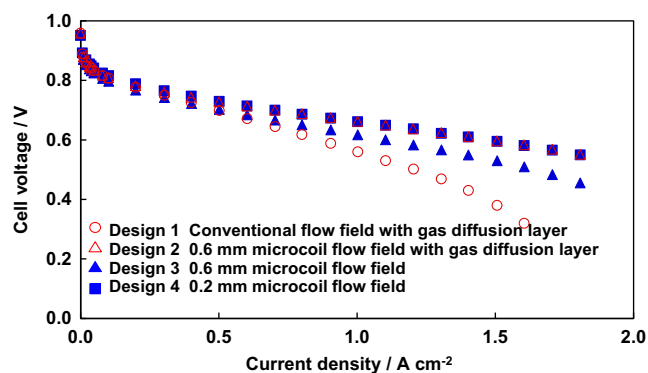

Fig. 4. Polarization curves for the microcoil without a GDL, the microcoil with a GDL, and the conventional flow field, obtained under $RH_{anode} = 100\%$, $RH_{cathode} = 100\%$, ambient pressure at the outlets, cell temperature = 70 °C, and hydrogen and air supplied in a stoichiometric ratio of 5.0 at 2.0 A cm^{-2}.

copper plates were used as material with known thermal conductivity (401 W m^{-1} K^{-1}), and the temperatures at the top and bottom of the copper plates were kept constant with water cooling condensers. A ceramic heater (MS-5, Sakaguchi EH VOC Corp., Tokyo, Japan) was placed between the upper and lower pairs of copper plates. The samples were placed in the middle of each pair of copper plates. Thermocouples were inserted in all the plates 1 mm from the samples. The compression pressure was precisely controlled and measured with a load cell (Kyowa, Tokyo, Japan); the uniformity of the pressure distribution on the surfaces of the plates was verified using Prescale film (for 0.5–2.5 MPa, Fujifilm Corporation, Tokyo, Japan) which indicated pressure intensity and distribution via color. The heater was controlled and monitored with an ampere meter to generate constant heat flux.

After 3 h, a steady state heat flux from the heater was equally transferred to the upper and lower pairs of copper plates, validated using the thermocouples in the copper plates without samples inserted. It was found that the copper plates located at equal distances from the heater were nearly the same temperature at compression pressures greater than 0.3 MPa. Above this compression pressure, the contact thermal resistance between the heater/copper plate and copper plate/copper plate boundaries were the same, as was the heat flux for the upper and lower pairs of plates. Therefore, all evaluations were conducted with a compression pressure of 1.0 MPa.

Square samples (25 mm × 25 mm) with unknown thermal conductivities were placed in the middle of each pair of plates (upper and lower). The heat flux for each sample was half of the total heat generated (50 W) from the heater. The temperatures of the bottom and top surfaces of the samples were calculated using the heat flux from the heater, the temperature of the copper plates, and the distance between the two thermocouples. The through-plane thermal resistance across the samples was determined via Fourier's law using the sample surface temperatures [22]. This measurement included the thermal resistance generated by the samples as well as the thermal contact resistance between the sample and the copper plates. By performing the experiment with samples of two different thicknesses, the intrinsic thermal conductivity and thermal contact resistance were determined.

We used two different thicknesses of commercially-available GDL to validate this measurement. We chose TGP-H-60 (190 μm thick, Toray, Tokyo, Japan) and TGP-H-90 (280 μm thick, Toray) to determine the intrinsic thermal conductivity. We compared this with product data released from Toray, as well as an evaluation of
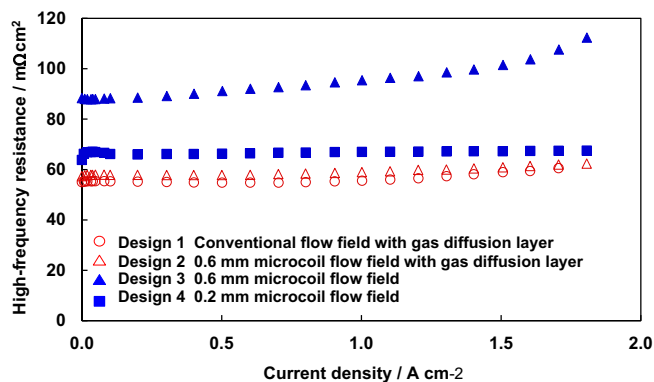
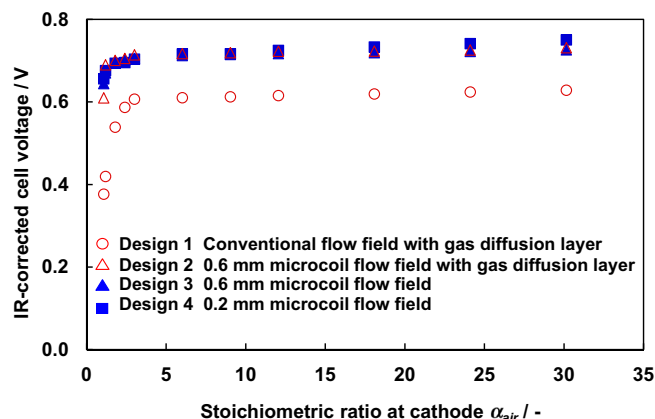**Fig. 5.** High-frequency resistance (HFR) for Designs 1–4.

the thermal conductivity for the GDL and the 0.2 and 0.6 mm microcoils used in our fuel cells.

3. Results and discussion

3.1. Polarization curves

Fig. 4 shows the polarization curves for Design 1 (conventional flow field with GDL), Design 2 (0.6 mm microcoil with GDL), Design 3 (0.6 mm microcoil), and Design 4 (0.2 mm microcoil). Fig. 5 shows the 1 kHz HFR, and Fig. 6 shows IR-corrected polarization curves for all four designs. IR correction is performed to compensate for the ohmic loss for each design using HFR and Fig. 6 shows the activation loss and the mass transfer loss (flooding) [23].

As seen in Fig. 6, all four IR-corrected polarization curves are nearly the same for the lowest current density tested, 0.3 A cm^{-2}. This indicates that the activation loss for each design is the same, that the gas is equally supplied to the catalyst in each design, and that the CCMs and MPLs have similar properties.

For Design 1, the cell voltage gradually decreases due to flooding as the current density exceeds 0.3 A cm^{-2} (Fig. 4), with a rapid voltage drop to 0.3 V at 1.7 A cm^{-2}. In contrast, the designs utilizing microcoils (Designs 2–4) exhibit flood-free performance even at a current density of 1.8 A cm^{-2}.

More significantly, the IR-corrected polarization curves for Designs 2 and 3 are identical (Fig. 6). This indicates that the GDL does not participate in the flooding mechanism, because Design 2 utilizes a GDL under the microcoils but its performance is flood-free.
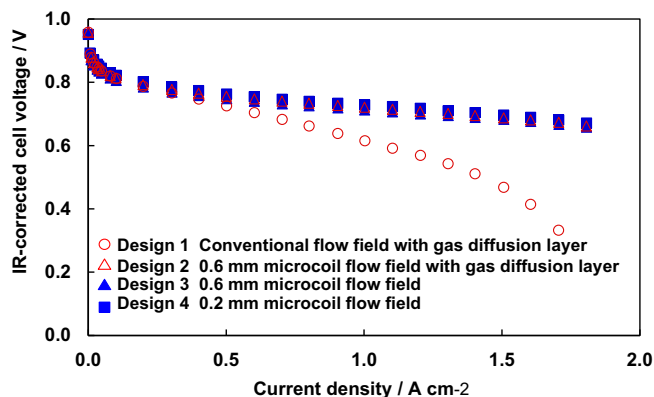

Fig. 6. IR-corrected polarization curves for the microcoils without a GDL, the microcoil with a GDL, and the conventional flow field.

Fig. 7. Dependence of IR-corrected cell voltage on cathode stoichiometry α_{air} for Designs 1–4.

This suggests that if gas is uniformly supplied to the active area with microcoils, a sufficient amount of gas reaches the catalyst layer without being blocked by water.

Higier and Liu have directly measured the location where flooding occurred in a conventional land/channel structure. They made two different membrane-electrode assemblies (MEAs) with Teflon sheets; one had an active area under just the lands, and the other had the active area under just the channel [24] using a Teflon sheet as a cover. They have found that the land-covered MEA exhibits flood-free performance, while the channel-covered MEA shows flooding, based on their polarization curve. Thus, the product water is not removed easily from under the land, preventing the cathode gas from diffusing into the catalyst layer. From a wider perspective of flow field structure, Design 2 is similar to the land-covered active area in Ref. [24], and therefore, the observed flood-free performance is reasonable.

P. Schulz et al. have demonstrated in their modeling work with a full morphology (FM) model that the liquid water in the GDL is transported along the gradient of capillary pressures [25]. They visualized a 3D liquid water network in a GDL using computational simulations. I.S. Hussaini and C.Y. Wang have recently characterized the water and air permeability for the GDL [26] for the through-plane and in-plane directions. They have shown that the air relative permeability decreases rapidly with increasing water saturation, while water relative permeability increases.

We were not certain that water saturation occurred during the operation of Design 2, and therefore, we could not specify the reason for the flood-free performance in this case. According to the rough assumption of the temperature in the GDL described in Section 3.3.2 (Fig. 10), the temperatures of the GDL for Designs 1 and 2 at 1 A cm^{-2} were estimated as 82.6 °C and 83.6 °C, respectively. These temperatures indicated that the condensation and evaporation rates for both designs were not very different and that liquid water might be present in the GDL for both designs. Although the studies noted above mention that low air permeability at high saturation could affect fuel cell performance, Design 2 exhibits flood-free performance. Presumably, the gas can travel through the GDL through the capillary fingering liquid water network [27]. It is unlikely that all the pores in the GDL are saturated, allowing diffusion of air. In addition, especially in Design 2, the gas could be supplied more uniformly to the top surface of GDL with microcoils, and almost all the surface was exposed to the gas flow without being plugged by the bipolar-plate; further, liquid water was thought to be removed more easily from the top surface of the GDL under
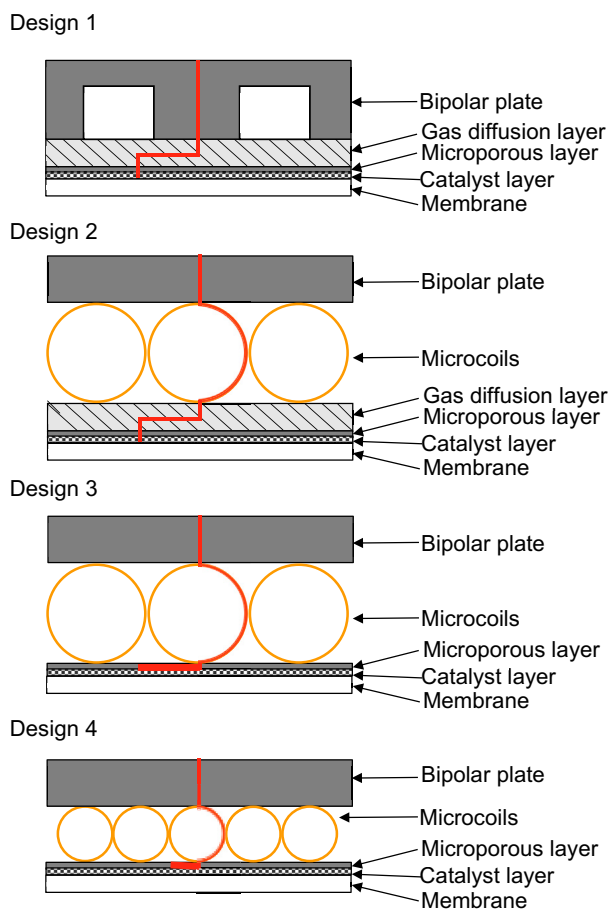
Fig. 8. Schematic of electrical conduction at the cathode in Designs 1–4.

Fig. 10. Estimated average temperature increase for Designs 1, 3, and 4. For the microcoil, thermal resistance data were used; for the GDL and MPL, thermal conductivity and thickness data were used to calculate the temperature increase.

dynamic gas flow along with the microcoils [28]. Therefore, in Design 2, the amount of liquid water in the GDL is probably kept lower, and the distribution of liquid water is kept more uniform, retaining the water saturation at a low level to allow for sufficient gas diffusion. This can be strongly influenced by the temperature and gas velocity, but further study is required for complete characterization (Fig. 9).
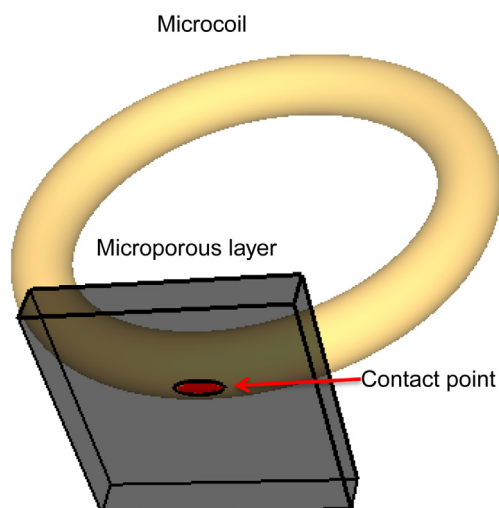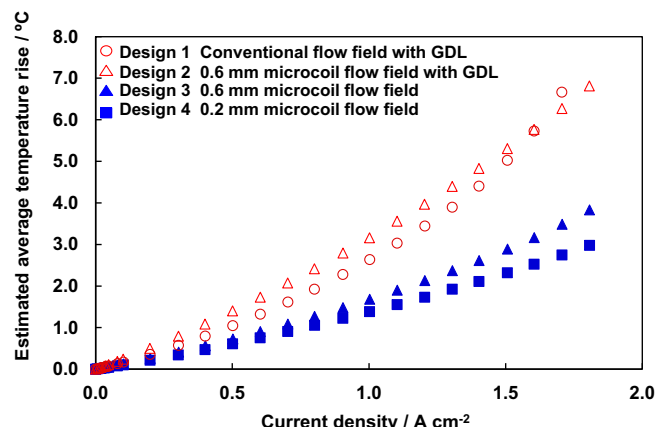

Fig. 9. Contact area represented with 3D CAD.

In Design 1, the accumulating water under the land cannot be removed because no gas flows over the water, as noted in Ref. [28]. Therefore, the pores under the land most probably suffer high water saturation that prevents gas penetration. In Designs 3 and 4, the microcoils are laid directly on the MPL without a GDL (Fig. 1). These designs exhibit nearly identical, flood-free performance. There is no space for water accumulation, and the forced convection causes movement of air in the coil directly against the water in the active area. The gas seems to be distributed uniformly onto the catalyst layer.

Further, the water in the MPL does not block air flow. It is thought that the water does not fill all the pores or create a liquid film in the MPL, because the pores are highly hydrophobic, being small and made of PTFE. Consequently, we conclude that flooding generation results from a combination of land/channel structure and the GDL.

3.2. Stoichiometry dependence

High cathode stoichiometry α_{air} is generally used to remove product water and prevent flooding [29], but this operation condition results in a significant reduction in system efficiency [30]. We have achieved flood-free operation using $\alpha_{air} = 9$ for 1.5 A cm^{-2} for Designs 2–4. In this section, we discuss the performance dependence on stoichiometry for all four designs.

Fig. 7 shows the dependence of cell voltage on cathode stoichiometry α_{air} for Designs 1–4 with a current density of 1 A cm^{-2} and 100% RH at 70 °C. Here, α_{air} is varied from 30 to 1.05 using an air mass flow controller. Design 1, with a conventional flow field, produces lower voltage than do Designs 2–3, which utilize microcoils, in the α_{air} range tested. Even with the higher stoichiometry at $\alpha_{air} > 10$, Design 1 suffers from flooding, and the performance begins to degrade at $\alpha_{air} = 3.0$, with more severe flooding [31]. This straight and parallel design leads to non-uniformity in air streams and catastrophic flooding at low air flow rates [32].

In contrast, the performances of Designs 2–4 are flood-free at $\alpha_{air} \geq 9.0$, as described in Section 3.1 and by the polarization curve in Fig. 4. Moreover, the performance does not degrade even at $\alpha_{air} = 1.2$.

The result for Design 1 indicate that the amount and distribution of liquid water in the GDL seems to be large or non-uniform to block gas diffusion in the GDL even under high stoichiometry at $\alpha_{air} > 10$; this water could not be removed and the

Table 2
In-plane and through-plane electron resistivity at 1 MPa compression pressure.

	In-plane	Through-plane
	Ω cm	Ω cm
Catalyst layer	9.9	2.9
MPL	2.5	9.8×10^{-1}
GDL	2.5×10^{-4}	7.3×10^{-4}

distribution could not be made uniform just by the stoichiometry under these conditions. A straight and parallel flow field is used with a channel width of 1 mm and a land width of 1 mm in Design 1 for the conventional flow field, which is thought to be the structure least amenable to the removal of water [33], but the land/channel structure might have a crucial defect.

In Designs 3 and 4 utilizing microcoils without a GDL, the results obtained are reasonable according to the same logic explaining the flood-free performance described in Section 3.1: direct flow for the entire active area without any liquid water transportation delay in the GDL, and ready air access to the catalyst without any gas diffusion delay in the GDL. Therefore, the cell voltage remains high even at a low stoichiometry value of $\alpha_{air} = 1.2$.

Design 2 exhibits high voltage at $\alpha_{air} = 1.2$, similar to Designs 3–4, even though it has a GDL. This indicates that the GDL does not affect the stoichiometry under these conditions. Since the voltage drop from flooding is larger under wetter conditions, such as 50 °C and 100% RH [34], the performance of Design 2 may decrease at higher stoichiometry.

3.3. High-frequency resistance (HFR)

3.3.1. HFR and electron conducting pathway

Fig. 5 shows the HFR for Designs 1–4. Designs 1 and 2 utilizing a GDL exhibit an HFR of 60–70 mΩ cm^2, in agreement with the values published in the literature [35–37]. Designs 3 and 4, which use microcoils directly on the MPL at the cathode, exhibit a relatively higher HFR. These results indicate that electrons can move from the MPL/catalyst-layer to the GDL because the GDL makes surface-to-surface contact with the entire active area, but the microcoils do not cover the entire active area and can make only point-to-surface contact. The microcoils are placed only on the MPL/catalyst layer in the interval of the coil diameter, meaning that the set of microcoils has fewer contact points with the MPL/catalyst layer.

Fig. 8 shows a schematic depicting the electron transfer from the catalyst layer to the bipolar plate. Table 2 shows the resistivity of the catalyst layer, MPL, and GDL in the in-plane and through-plane directions. The assumptions shown in Fig. 8 indicate that each design has a different electron transfer pathway from the catalyst to the bipolar plate. In Designs 1 and 2, electrons in the land of the bipolar plate coming from an external load first travel horizontally in the GDL, then move vertically to the MPL, and move vertically to the catalyst layer under the channel. In contrast, in Designs 3 and 4, the electrons in the microcoil travel horizontally in the MPL and then move vertically to the catalyst layer between the microcoils. The resistivity of the MPL is 10^4 times larger than that of the GDL (Table 2), meaning that Designs 3 and 4 probably suffers larger ohmic losses due to in-plane MPL resistance, resulting in a higher HFR than that in Designs 1 and 2.

Even though Designs 3 and 4 are both essentially microcoils without a GDL, the HFR of Design 3 is higher than that of Design 4. This result can be explained by the distance of the in-plane MPL electron-conducting pathway. Design 3 uses 0.6 mm microcoils and Design 4 uses 0.2 mm microcoils, introducing a difference in the diameter that affects the distance traveled by electrons transferred

through the MPL in the in-plane direction, thus incurring ohmic loss along the MPL. Although the in-plane MPL distance in Design 3 is three times that in Design 4, the HFR of Design 3 is only 1.4 times larger than that of Design 4.

This discrepancy arises because the electron resistance between the MPL and the microcoil were formed by point-contact. In such a case, the contact resistance could not be explained by the length of the electron-conducting pathway but by the number of contact points and the spot area of a single contact point. R. Holm investigated the point-contact resistance between a flat pate and the contact points equally dispersed in a specific area A [38]. They found that the resistance R_C can be expressed as

$$R_C = \frac{\rho \sqrt{\pi}}{4\sqrt{S}\sqrt{N}} \tag{1}$$

where ρ is the electric resistivity of a flat plate, S is the total contact area of the actual contact point, and N is the number of contact points. In Designs 3 and 4, the contact points between the MPL and the microcoils were dispersed in the same active area A_{Active} and the conductivities of the MPL ρ_{MPL} were the same for each design. The area of the single contact point formed between the MPL and the lower end of the microcoil is not accurately known, but we assumed that the compression pressure of the fuel cell could press the microcoil down on the MPL and that the microcoil fiber would sink into the MPL to a depth of 1 μm. The MPL should be flexible enough to make the contact with the entire 1 μm depth of the microcoil fiber. We used 3D CAD to calculate the contact area, as shown in Fig. 9. The area of the single point contact for Designs 3 and 4 was 764 μm^2 and 443 μm^2, respectively. The number of contact points N for Design 3 and Design 4 was 9435 and 27,750, respectively. Therefore, the total contact area of the actual contact points in Designs 3 and 4 was 7.2 mm^2 and 12.3 mm^2, respectively. According to Equation (1), the contact resistance of Design 3 is 2.2 times larger than that of Design 4. The value does not agree with the actual HFR values.

The discrepancy may be due to the area of the single contact point because we did not measure this and assumed the 1 μm depth contact of the microcoil with the MPL, and this did not represent the actual contact area. For further studies, we need to obtain the mechanical properties of the MPL and determine the actual contact area by performing experiments or computational calculations, for example, using a finite element model (FEM). However, consideration of the point contact between the microcoil and the MPL is thought to be significant even with the aforesaid discrepancy.

3.3.2. HFR and membrane dry-out

During PEFC operation, water is produced by the oxygen reduction reaction at the cathode, leading to a higher water concentration at the cathode than that at the anode. Water thus diffuses from the cathode to the anode so as to equilibrate the concentrations between the two compartments. This phenomenon is widely known as back diffusion [10]. At the same time, the water at the anode moves to the cathode along with proton transfer through the membrane because the protons are encapsulated by solvation shells, meaning that proton transfer results in net water transfer as well. This phenomenon is known as electro-osmotic drag [39]. At low current densities, back diffusion prevails over electro-osmosis, while the opposite is true at high current densities, meaning that the anode tends to dry out even if the cathode is well hydrated [40]. The membrane resistivity strongly depends on the water content of the membrane, and thus, membrane dehydration can cause increased HFR.

Fig. 5 reveals that the HFR for all the designs increases with increasing current density. However, the nature of the increased

Table 3
Through-plane thermal resistance and thermal conductivity of the GDL, the microcoil, and the MPL at 1 MPa compression pressure.

	Measured thermal resistance	Measured thermal conductivity	Reported thermal conductivity
	$m^2 \ K \ W^{-1}$	$W \ m^{-1} \ K^{-1}$	$W \ m^{-1} \ K^{-1}$
GDL (TGP-H-060, 190 μm)	5.1×10^{-4}	1.7	1.80 ± 0.27 [42]
GDL (TGP-H-090, 280 μm)	5.6×10^{-4}		
Microcoils (200 μm)	2.6×10^{-4}	–	–
Microcoils (600 μm)	3.3×10^{-4}		
Stainless Steel (SUS316)	–	–	16.7
MPL (40 μm)	2.2×10^{-4}	0.04	0.3 [21]
MPL (60 μm)	6.7×10^{-4}		

HFR is different for each design. The HFR for Designs 1 and 2, utilizing a GDL, is similar and starts to increase slightly at a current density of 1.2 A cm^{-2}, from 55 to 60 mΩ cm^2. The HFR for Design 3, however, starts to increase earlier, at 0.3 A cm^{-2}, from 90 to 120 mΩ cm^2. Finally, the HFR for Design 4 increases only slightly, from 66 to 67 mΩ cm^2.

M.M. Mench et al. [41] and S. He et al. [42] have mentioned that the increase in the electrolyte membrane temperature from the initial temperature at the open circuit is 12–15 °C at a current density of 1 A cm^{-2}, which can cause membrane dehydration. In our study, we have not measured the membrane temperature, monitoring only the bipolar temperature (80–81 °C) for all the designs through the current density range. Hence, we have been unable to estimate the HFR increase based on the membrane temperature. Instead, we have evaluated the thermal resistance for the GDL, the microcoil and the MPL, as described in Sections 2–4, to evaluate whether these thermal resistances affect the membrane temperature through heat transfer from the membrane to the bipolar plate, the temperature of which is maintained at 80 °C using a sheet-heater and thermocouples.

Table 3 shows the thermal resistance of the 190 μm TGP-H-060 GDL and the 280 μm TGP-H-090 GDL, as well as the 0.6 and 0.2 mm microcoils. The thermal conductivity of the GDL is also calculated using the thermal resistances for the different thicknesses in order to confirm the reasonableness of the measurement, comparing the data obtained with that from manufacturer's data sheet.

The thermal conductivity of the GDL is 1.7 W m^{-1} K^{-1}, agreeing well with the value listed in the literature, 1.80 ± 0.27 W m^{-1} K^{-1} (Table 3) [43], giving us confidence in the accuracy of our results. It is difficult to measure and calculate the thermal conductivity of the microcoils due to the two different diameters used. Unavoidably, the thermal resistance also reflects the contact resistance of copper plate (Fig. 3). However, we use the thermal resistance data to estimate the temperature rise in the membrane.

Using the thermal conductivity data for the GDL and the MPL as well as based on the two different thicknesses tested, in addition to the thermal resistance data of the microcoils (Table 3), the temperature increase in the membrane is estimated under the following assumptions:

(1) uniform heat generation in the active area
(2) uniform heat transfer to the next layer only in the through-plane direction
(3) heat generation calculated with $I \bullet (E_{th} - E_{cell})$. I: cell current, E_{th} is thermoneutral voltage (HHV), E_{cell} is cell voltage

(4) the heat divided equally to the cathode and anode
(5) generated water removed as liquid
(6) no heat generation in the MPL, GDL, or microcoil
(7) no contact heat resistance
(8) no secondary heat transfer or conduction
(9) constant bipolar temperature
(10) constant thermal conductivity in the temperature range used in this estimation

For the assumption (3), there are basically four sources of heat generation in a PEMFC, namely the entropic heat of reactions, the irreversible heat of electrochemical reactions, heat from the ohmic resistances and heat from the condensation of water vapor [44]. E_{th} is known as the thermoneutral voltage [45], which represents the imaginary maximum voltage of a fuel cell assuming all the 4 energies is converted to the electric energy. E_{cell} and I are the cell operating voltage and the current. Here E_{th} includes the released energy of the product water to be the liquid phase, based on the higher heating value (HHV) because the product water assumed to be removed at this time as the assumption (5), and the corresponding values for the HHV is 1.48 V [46].

Fig. 10 shows the temperature increase in the CCM. Design 1, featuring a conventional flow field, produces results similar to those obtained by M.M. Mench [41]; however, the results also reveal that the temperature increases of Designs 1 and 2 utilizing the GDL are twice those of Designs 3 and 4, and in addition, the range of temperature increase in Designs 3 and 4 is similar. This result provides discrepant explanations for the differences in the HFR increase in Fig. 5. The HFR increase in the case of Designs 1 and 2 was small and that in Design 3 was the highest, but the temperature increases were not similar to the HFR increases. This result is not unreasonable because the thermal resistances for Designs 1–4 under assumptions (1)–(10) are 1.57, 2.22, 1.09, and 0.97 °C W^{-1}, respectively, and these are on the similar order as the temperature increase estimated in Fig. 10.

According to the HFR increase in Fig. 5, the temperature increase should be in the order Design 3 > Design 2 ≃ Design 1 > Design 4, but the estimated temperature increase is in the order Design 2 > Design 1 > Design 3 > Design 4. This indicates that the thermal resistance of Design 3 with the 0.6-mm microcoil should be underestimated under the assumptions, especially assumption (2), which is uniform heat transfer only in the through-plane direction. In the actual fuel cells with 0.6-mm microcoils, heat is transferred in-plane in the MPL between the two coils, and these contacts are formed by point-contact, similar to the electron conduction path described in Section 3.3.1. Unfortunately, the experiment depicted in Fig. 2 should underestimate the effect of horizontal conduction because the thermal conductivity of copper is three times greater in magnitude than the MPL, implying that the copper-plate/microcoil system should have a much lower thermal resistance than the MPL/microcoil system. In future studies, we will estimate the thermal resistance of the MPL/microcoil system. In addition, we will calculate the temperature rise in the fuel cell via 3D FEM with non-isotropic thermal conductivity of the MPL, contact thermal resistance against the load pressure of the end plates, and coupling of electron conduction with ohmic heat generation in the MPL and other elements of the fuel cell.

4. Conclusions

In this study, we characterized the IV performance, stoichiometry performance, and HFR for microcoil fuel cells. Electrical conductivities for each element were measured to explain the HFR difference between the microcoil fuel cells and the conventional fuel cell, and thermal conductivities were also measured to

S. Tanaka, T. Shudo / Journal of Power Sources 248 (2014) 524–532

elucidate the behavior of HFR against current density with a simple estimation. The main conclusions drawn from this study are as follows:

1. Microcoil fuel cells exhibit flood-free performance.
2. From the comparison among the microcoil, microcoil with a GDL, and a grooved flow field with a GDL, only the latter exhibited flooding because the non-uniform structure promoted non-uniform gas distribution and water accumulation. The GDL itself had little or no observable effect on either the IV or stoichiometry performance.
3. The HFR of the microcoils without a GDL was higher than that of the microcoil with a GDL, due to differences in the electron conduction path. Electrons were conducted horizontally in the in-plane direction in the MPL, and in-plane electron conductivity is key to enhancing microcoil fuel cell performance.
4. The temperature increase with uniform heat transfer only in the through-plane direction could not represent the actual microcoil fuel cell, with underestimation of the thermal resistance between the MPL and the microcoil, similar to electron conductivity.

In future studies, we will calculate the voltage drop through the electron conductivities of the fuel cell components and the contact resistances between these components under a certain compression pressure of the end plates, via 3D FEM. We will prepare several conductive MPL samples and test them in the fuel cell to validate the calculations.

In addition, we will calculate the temperature rise in the fuel cell via 3D FEM with non-isotropic thermal conductivity of the MPL, contact thermal resistance against the load pressure of the endplates, and coupling of electron conduction with ohmic heat generation in the MPL and other elements of the fuel cell.

Acknowledgments

Glossary

CB	carbon black
CCM	catalyst-coated membrane
IV	current–voltage
DMFC	direct methanol fuel cell
EIS	electrical impedance spectroscopy
EPDM	ethylene–propylene diene monomer rubber
FEM	finite element model
FM	full morphology
GDL	gas diffusion layer
HFR	high frequency resistance
MEA	membrane-electrode assembly
MPL	microporous layer
PEFC	polymer electrolyte fuel cell
PTFE	polytetrafluoroethylene
PEM	proton exchange membrane
RH	relative humidity

References

[1] P.L. Hentall, J.B. Lakeman, G.O. Mepsted, P.L. Adcock, J.M. Moore, J. Power Sources 80 (1999) 235–241.
[2] K. Jiao, B. Zhou, J. Power Sources 169 (2007) 296–314.
[3] C. Bao, M. Ouyang, B. Yi, Int. J. Hydrogen Energy 31 (2006) 1879–1896.
[4] T.V. Nguyen, ECS Trans. 3 (2006) 1171–1180.
[5] Transitions to Alternative Transportation Technologies—a Focus on Hydrogen, The National Academies Press, Washington, D.C., 2008.
[6] C.C. Chan, Proc. IEEE 90 (2002) 247–275.
[7] M. Arita, Fuel Cells 2 (2002) 10–14.
[8] X.G. Yang, F.Y. Zhang, A.L. Lubawy, C.Y. Wang, Electrochem. Solid-State Lett. 7 (2004) A408–A411.
[9] J.T. Pukrushpan, H. Peng, A.G. Stefanopoulou, J. Dyn. Sys., Meas. Control 126 (2004) 14–25.
[10] N. Yousfi-Steiner, Ph. Moçotéguy, D. Candusso, D. Hissel, A. Hernandez, A. Aslanides, J. Power Sources 183 (2008) 260–274.
[11] W. Dai, H. Wang, X.-Z. Yuan, J.J. Martin, D. Yang, J. Qiao, J. Ma, Int. J. Hydrogen Energy 34 (2009) 9461–9478.
[12] H. Li, Y. Tang, Z. Wang, Z. Shi, S. Wu, D. Song, J. Zhang, K. Fatih, J. Zhang, H. Wang, Z. Liu, R. Abouatallah, A. Mazza, J. Power Sources 178 (2008) 103–117.
[13] T.A. Zawodzinski Jr., C. Derouin, S. Radzinski, R.J. Sherman, V.T. Smith, T.E. Springer, S. Gottesfeld, J. Electrochem. Soc. 140 (1993) 1041–1047.
[14] T. Shudo, K. Suzuki, Int. J. Hydrogen Energy 33 (2008) 2850–2856.
[15] D.G. Strickland, J.G. Santiago, J. Power Sources 195 (2010) 1667–1675.
[16] A. Turhan, K. Heller, J.S. Brenizer, M.M. Mench, J. Power Sources 180 (2008) 773–783.
[17] M. Mathias, J. Roth, J. Fleming, W. Lehnert, in: W. Vielstich, H. Gasteiger, A. Lamm (Eds.), Handbook of Fuel Cells: Fundamentals, Technology and Applications, vol. 3, John Wiley & Sons, New York, 2003.
[18] T.E. Springer, T.A. Zawodzinski, M.S. Wilson, S. Gottesfeld, J. Electrochem. Soc. 143 (1996) 587–599.
[19] N. Cunningham, M. Lefèvre, G. Lebrun, J.-P. Dodelet, J. Power Sources 143 (2005) 93–102.
[20] G. Karimi, X. Li, P. Teertstra, Electrochim. Acta 55 (2010) 1619–1625.
[21] G. Unsworth, N. Zamel, X. Li, Int. J. Hydrogen Energy 37 (2012) 5161–5169.
[22] F.P. Incropera, D.P. DeWitt, Fundamentals of Heat and Mass Transfer, fourth ed., John Wiley & Sons, New York, 1996.
[23] M.V. Williams, H.R. Kunz, J.M. Fenton, J. Electrochem. Soc. 152 (2005) A635–A644.
[24] A. Higier, H. Liu, J. Power Sources 193 (2009) 639–648.
[25] V.P. Schulz, J. Becker, A. Wiegmann, P.P. Mukherjee, C.-Y. Wang, J. Electrochem. Soc. 154 (2007) B419–B426.
[26] B. Ramos-Alvarado, J.D. Sole, A. Hernandez-Guerrero, M.W. Ellis, J. Power Sources 218 (2012) 221–232.
[27] E. Aker, K. Jørgen Måløy, A. Hansen, G.G. Batrouni, Transp. Porous Media 32 (1998) 163–186.
[28] B.A. McCain, A.G. Stefanopoulou, I.V. Kolmanovsky, Chem. Eng. Sci. 63 (2008) 4418–4432.
[29] W.R. Mérida, G. McLean, N. Djilali, J. Power Sources 102 (2001) 178–185.
[30] R.S. Gemmen, C.D. Johnson, J. Power Sources 159 (2006) 646–655.
[31] N. Pekula, K. Heller, P.A. Chuang, A. Turhan, M.M. Mench, J.S. Brenizer, K. Ünlü, Nucl. Instrum. Methods Phys. Res. A 542 (2005) 134–141.
[32] T.V. Nguyen, J. Electrochem. Soc. 143 (5) (1996) L103–L105.
[33] X. Li, I. Sabir, J. Park, J. Power Sources 163 (2007) 933–942.
[34] A. Hakenjos, H. Muenter, U. Wittstadt, C. Hebling, J. Power Sources 131 (2004) 213–216.
[35] J.P. Owejan, T.A. Trabold, D.L. Jacobson, D.R. Baker, D.S. Hussey, M. Arif, Int. J. Heat Mass Transf. 49 (2006) 4721–4731.
[36] S.J.C. Cleghorn, D.K. Mayfield, D.A. Moore, J.C. Moore, G. Rusch, T.W. Sherman, N.T. Sisofo, U. Beuscher, J. Power Sources 158 (2006) 446–454.
[37] Jon P. Owejan, Jeffrey J. Gagliardo, Jacqueline M. Sergi, Satish G. Kandlikar, Thomas A. Trabold, Int. J. Hydrogen Energy 34 (2009) 3436–3444.
[38] R. Holm, Electric Contacts, fourth ed., Springer, New York, 1967.
[39] J. Larminie, A. Dicks, Fuel Cell System Explained, first ed., John Wiley & Sons, New York, 2000.
[40] P. Sridhar, Ramkumar Perumal, N. Rajalakshmi, M. Raja, K.S. Dhathathreyan, J. Power Sources 101 (2001) 72–78.
[41] M.M. Mench, D.J. Burford, T.W. Davis, in: Proceedings of IMECE '03 International Mechanical Engineering Congress and Exposition, Washington, D.C., Nov. 16–21, 2003.
[42] S. He, M.M. Mench, S. Tadigadapa, Sens. Actuators A Phys. 125 (2006) 170–177.
[43] M. Khandelwal, M.M. Mench, J. Power Sources 161 (2006) 1106–1115.
[44] H. Ju, H. Meng, C.-Y. Wang, Int. J. Heat Mass Transf. 48 (2005) 1303–1315.
[45] X. Li, Principles of Fuel Cells, Taylor & Francis, New York, 2006.
[46] R. O'Hayre, S.-W. Cha, W. Colella, F.B. Prinz, Fuel Cell Fundamentals, second ed., John Wiley & Sons, New York, 2009.